Stable Organic Thermoelectric Devices for Self–Powered Sensor Applications

Journal:	*Journal of Materials Chemistry A*
Manuscript ID	TA-PER-09-2020-008598.R1
Article Type:	Perspective
Date Submitted by the Author:	10-Oct-2020
Complete List of Authors:	Mukaida, Masakazu; Advanced Industrial Science and Technology Tsukuba Research Headquarters Central Kirihara, Kazuhiro; National Institute of Advanced Industrial Science and Technology (AIST), Horike, Shohei; National Institute of Advanced Industrial Science and Technology (AIST), Nanomaterials Research Institute Wei, Qingshuo; National Institute of Advanced Industrial Science and Technology (AIST), Nanosystem Research Institute (NRI)

SCHOLARONE™
Manuscripts

PERSPECTIVE

Stable Organic Thermoelectric Devices for Self-Powered Sensor Applications

Masakazu Mukaida,*[a,b] Kazuhiro Kirihara,*[a,b] Shohei Horike[a,c] and Qingshuo Wei*[a,b,c]

The feasibility of using organic thermoelectric devices to power sensors for different applications is a critically encouraging factor for researchers. Organic semiconductors indeed possess lower thermoelectric performance than their inorganic counterparts; however, these can be compensated with certain advantages such as their lightweight, low fabrication cost, and low fabrication temperature. For practical applications, they face competition with Li ion batteries, which are known for their high energy density and long lifetime. Thus, in addition to the corresponding power output, the ideal organic thermoelectric devices require excellent stability. In this study, we examined such a perspective by primarily focusing on recent studies on organic thermoelectric devices concerning their practical applications. The impact of contact resistance on the device performance has been discussed, along with suggestions of certain promising device structures for organic thermoelectric devices. Experimentally, we confirmed that light and compact organic thermoelectric devices with a size ~10 cm^2 should be sufficiently good to power the sensors. Moreover, these devices were confirmed to operate under natural cooling conditions without a heat sink, thus showing excellent stability for >70 days under a continuous working condition at 100°C.

1. Introduction

As the Internet of Things (IoT) evolves, billions of sensors are expected to be embedded in the virtual environment connected by computing systems, software, and services to impact our daily lives,[1] especially for monitoring applications in infrastructure, factory environment, and health industries. Sensors for internet applications, however, have recognizable setbacks. In addition to the sensor part, the power source can sometimes be an issue, e.g., electrical wirings is not a smart choice for wireless sensors. Batteries could power the sensors, but constantly replacing or charging expired batteries may complicate the supply generation process. One good solution is to develop self-powered sensors that harvest energy from the outside environment.[2–4] Different energy techniques can be used to harvest and use energy from known sources such as light, EM radiation, heat, vibration, motion, and magnetic strength.[5,6] Unlike such sources, thermal energy is distributed almost everywhere. It is reported that the achievable energy density with thermal energy ranges from $\mu W/cm^2$ to mW/cm^2, which matches the energy consumption of sensors.[7,8]

Thermoelectric devices have been studied for their potential suitability to directly convert heat into electricity for sensor applications, practically because of the absence of moving parts that could make them compact and reliable.[9] Early research works concerning thermoelectric materials primarily focused on inorganic semiconductors such as Bi–Te alloys, Mg–Si alloys, and metal oxides.[10–15] These materials mostly exhibit good performance at temperatures of >200°C, although the waste heat in the environment is usually at temperatures of <150°C. The most common low-temperature thermoelectric material used is Bi_2Te_3. However, because Te is an expensive rare metal and not environmentally friendly, its production may be unsuitable for large-area applications. Furthermore, because inorganic thermoelectric devices are typically fabricated by a sintering process at high temperatures, the energy payback could be challenging to achieve. In this sense, utilizing heat to fabricate self-powered sensors demands eco-friendly thermoelectric devices.

Organic thermoelectric materials and devices have recently become a recognizable topic in the research community.[7,16–25] Although organic materials have been known to demonstrate lower thermoelectric performance than their inorganic counterparts, certain characteristics they possess, such as lightweight (the density of organic materials is typically ~1 g/cm^3, that of Bi_2Te_3 is ~8 g/cm^3)[26,27], low environmental impact, and flexibility, give them a critical advantage for applications into self-powered sensors. Unfortunately, there are not so many studies on device fabrication and identifying the added value of organic thermoelectric devices. In this report, we highlight recent pioneering studies revolving on the

[a.] Nanomaterials Research Institute, Department of Materials and Chemistry, National Institute of Advanced Industrial Science and Technology (AIST), 1-1-1 Higashi, Tsukuba, Ibaraki 305-8565 Japan. E-mail: mskz.mukaida@aist.go.jp, kz-kirihara@aist.go.jp, qingshuo.wei@aist.go.jp

[b.] AIST-UTokyo Advanced Operando-Measurement Technology Open Innovation Laboratory (OPERANDO-OIL), National Institute of Advanced Industrial Science and Technology, 1-1-1 Higashi, Tsukuba, Ibaraki 305-8565 Japan

[c.] Precursor Research for Embryonic Science and Technology (PRESTO), Japan Science and Technology Agency, 4-1-8 Honcho, Kawaguchi, Saitama 332-0012, Japan

practical applications of organic thermoelectric devices. The primary topic is not the material properties; however, on several contemporary organic thermoelectric materials that have been developed. A discussion on the effect of contact resistance on the device performance is provided, along with suggestions of a possible approach to reduce the contact resistance. Several promising device structures for organic thermoelectric devices will be increased, especially on considerations of the anisotropicity of material properties, heat flow directions, and cooling mechanisms. In the later sections, we will discuss the stability of organic thermoelectric devices and demonstrate that a compact organic thermoelectric module based on self-power sensors could have excellent durability.

2. Material Properties

Organic semiconductors possess certain thermoelectric properties, such as the Seebeck effect, which have long been studied with the development of organic conductors. In organic conducting materials, the Seebeck effect is a physical parameter used to determine the carrier type and relative carrier concentration.[28] With the recent efforts in developing organic electronics, the physical and chemical properties of organic conducting polymers have improved such that they can now tune over a wide range, making them suitable for thermoelectric applications.[16,26,29–38]
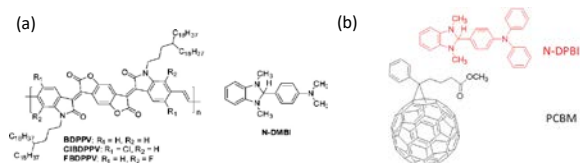

Figure 1. (a) Chemical structures of BDPPV derivatives and *n*-type dopant N-DMBI. Reproduced with permission from [49] Copyright 2015 American Chemical Society. (b) Chemical structures of PCBM and *n*-type dopant N-DPBI. Reproduced with permission from [48] Copyright 2018 Wiley.

Similar to inorganic thermoelectric materials, the organic ones can either be p-type or n-type. N-type organic thermoelectric materials are relatively limited given the significant challenges they face to achieve efficient doping and stability toward moisture and oxygen.[39–44] Nevertheless, several pioneering studies demonstrated certain promising thermoelectric properties of the n-type organic thermoelectric materials via molecular doping. [39–41,45–56] For example, Pei et al. synthesized a series of benzodifurandione-based poly(p-phenylene vinylene) (BDPPV) derivatives that exhibit electron mobility of up to 1.70 cm^2/(Vs) under ambient conditions (Figure 1a).[52] The low LUMO levels in these polymers caused the efficient electron transfer from dihydro-1H-benzoimidazol-2-yl (N-DBI), whereas spin-coating the BDPPV/N-DBI mixture allowed a σ of 14 S/cm and power factors up to 28 μW/(m^{-}K^2) in thin solid films. Kemerink et al. developed an inverse-sequential doping method for C$_{60}$ derivative using 4-(1,3-dimethyl-2,3-dihydro-1H-benzimidazol-2-yl)-N,N-

diphenylaniline (N-DPBI), resulting in a high power factor of 35 μW m^{-1} K^{-2} under a high conductivity of 40 S cm^{-1} (Figure 1b)[51]. Unlike the n-type thermoelectric materials, the p-type ones are abundant. They could generally be divided into two groups: poly(3,4-ethylenedioxythiophene)-based materials (Figure 2a) which are doped during the polymerization,[57–65] and the others, which generally are nonconductive and can be molecularly doped after film formation.[66,67]

The high σ in highly doped poly(3,4-ethylenedioxythiophene) (PEDOT) is responsible for its respective thermoelectric performance.[68,69] The typical Seebeck coefficient is not high in this material with only 11 μV/K for in situ polymerized PEDOT thin films[60] and ~17 μV/K for PEDOT:PSS[33], most likely because of the high carrier density in these materials.[70,71] Some attempts were made to further improve the thermoelectric properties in these materials, such as controlling the carrier density inside the films, which is a typical approach in the field of inorganic thermoelectric materials.[32,72,73] In their pioneering study, Crispin et al. on the de-doping of poly (3,4-ethylenedioxythiophene):tosylate (PEDOT:tos) observed a figure-of-merit (*ZT*) of 0.25 primarily attributed to a high S (>200 μV/K).[32] In their latter studies, they highlighted the difficulties of in-plane thermal conductivity (κ) measurements.[74] They accurately estimated the maximum *ZT* (0.11) for PEDOT:tos at an oxidation level of ~22% at room temperature. We used a solid-state photoinduced charge-transfer reaction to precisely control the carrier density in poly (3,4-ethylenedioxythiophene):poly (styrenesulfonate) (PEDOT:PSS) films. We demonstrated that the Seebeck coefficient measured as a function of the irradiation time reveals a maximum power factor of ~42 μW/mK^2 at a carrier density of ~5 × 10^{20} cm^{-3},[75] while the estimated *ZT* was ~0.02. Such an approach could provide a possible route to finely control and measure the doping density of a single device.

Other organic semiconductors could be chemically doped by exposing them to oxidative agents or acids such as Fe^{3+}, I$_2$, 7,7,8,8-tetracyano-2,3,5,6-tetrafluoroquinodimethane (F$_4$TCNQ), and toluenesulfonic acid after the film formation.[66,67,76–82] For a high σ via molecular doping, both doping density and carrier mobility must be considered: a high concentration of dopants could generate more charges; moreover, it could affect the molecular packing and the morphology, decreasing the carrier mobility. Kang et al. developed a doping process by evaporating F$_4$TCNQ molecules on top of a liquid crystal polymer poly(2,5-bis(3-hexadecylthiophen-2-yl)thieno[3,2-b]thiophene (PBTTT) layer, which allowed the polymer to retain its highly ordered lamellar microstructure with the dopant incorporated into the layer of side chains (Figure 2b).[83,84] This solid-state diffusion method allowed a σ that was considerably higher than 200 S/cm. Patel et al. studied and compared the thermoelectric properties of (tridecafluoro-1,1,2,2-tetrahydrooctyl)trichlorosilane (FTS) doped PBTTT and observed better thermoelectric performance (with a Seebeck coefficient of ~33 μV/K and a power factor of 100 μW/(mK^2)), exceeding that of films doped with 4-ethylbenzenesulfonic acid (Figure 2c).[85,86] Interestingly, this difference was not caused by local structure perturbations
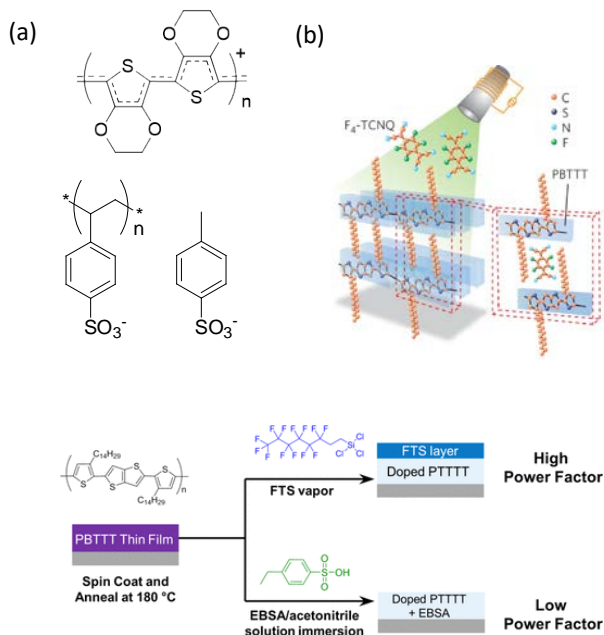
Figure 2. (a) Chemical structures of the molecular structures of poly(3,4-ethylenedioxythiophene) (PEDOT), poly(styrenesulfonate) (PSS), and tosylate (tos). (b) Schematic of the doping method showing the evaporation procedure of F$_4$-TCNQ and the resulting edge-on stacking of PBTTT with F$_4$-TCNQ molecules diffusing into the interdigitated side-chain region. Reproduced with permission from [80] Copyright 2016 Springer. (c) The vapor and solution routes for the treatment of PBTTT. Reprinted with permission from [83]. Copyright 2016 American Chemical Society.

induced by the dopants but by changes in carrier scattering in the disordered regions of the film and probably the entropic vibrational component of the Seebeck coefficient. Furthermore, they compared the thermoelectric properties of a series of semiconducting polymers (with an σ of 10^{-5}–1000 S/cm) doped with either F$_4$TCNQ or FTS, but did not identify any noticeable maximum in the power factor of these polymers unlike what is typically observed for inorganic semiconductors.[87]

Hybrid materials using organic and inorganic thermoelectric materials have been studied. There are several expected effects of using hybrid materials other than conducting polymers or inorganic TE materials, such as improved electrical conductivity because of polymer ordering, and an increased Seebeck coefficient through interface scattering and reduced thermal conductivity compared with inorganic TE materials. There are numerous studies of PEDOT/inorganic hybrid composites such as PEDOT/Te,[88] PEDOT/PbTe,[89] PEDOT/Bi$_2$Te$_3$,[90] and PEDOT/Ge.[91] Please note both the electrical conductivity and Seebeck coefficient of the films could decrease if a homogeneous mixture of the materials cannot be obtained. This is because carriers flow through each material independently.

3. Contact Resistance

Thermoelectric devices can be fabricated by connecting the semiconductor in series or parallel using a metal electrode. In the process, the contact resistance between the conducting polymer and the metal electrode could substantially affect the device performance because it contributes to the internal resistance of the devices. However, studies exploring how the contact resistance affect the thermoelectric performance of the organic devices are rare.

We could estimate the effect of the contact resistance on thermoelectric conversion efficiency using thermoelectric parameters from PEDOT:PSS to calculate the power output of one leg. Here, we assume a flat interface and consider the thermoelectric power output of one leg of area A and thickness L. Figure 3a shows a schematic of the device used for the calculation.

When the metal electrode plates are connected to the upper and the lower sides of the element and temperature gradient ΔT is applied along the through-plane direction of the component, we obtain a maximum power density P given by

$$P = \frac{1}{4} \times \frac{(S\Delta T)^2}{R_1 + 2R_c} \times \frac{1}{A}, \qquad (1)$$

where S is the Seebeck coefficient, R_1 is the resistance of the element, and R_c the contact resistance between the element and the metal electrodes. The electrical conductivity σ of PEDOT/PSS and the contact resistivity r_c ($R_c = r_c/A$) can be utilized to obtain

$$P = \frac{1}{4} \times \frac{(S\Delta T)^2}{\frac{1}{\sigma} \times \frac{L}{A} + 2 \times \frac{r_c}{A}} \times \frac{1}{A} \qquad (2)$$

$$P = \frac{1}{4} \times \frac{(S\Delta T)^2}{L/\sigma + 2r_c} \qquad (3)$$

From equation (3), we can see that the power density of the device is not related to the contact area but the device thickness. In the simplified case, for 1D heat conduction, the thermal resistance K_1 from the device can be represented as follows:

$$K_1 = \frac{1}{\kappa} \times \frac{L}{A}, \qquad (4)$$

where κ is the thermal conductivity of the leg (Here we used the thermal conductivity of PEDOT/PSS.). The heat transfer efficiency at the air/device surface was assumed at $h_i = 100$ W/m^{2}K (moderate speed flow of air over a surface).[92] Accordingly, the thermal resistance K_i at the device/air interface is

$$K_i = \frac{1}{h_i A} \qquad (5)$$

Considering that the temperature of the hot side was 100°C and the environmental temperature was 20°C,

$$\Delta T = \frac{K_1}{K_1 + K_i} \times (100 \,°C - 20°C); \qquad (6)$$

$$\Delta T = \frac{L/\kappa}{L/\kappa + 1/h_i} \times 80; \qquad (7)$$

$$P = \frac{1}{4} \times \frac{(S \times (\frac{L/\kappa}{L/\kappa + 1/h_i} \times 80))^2}{L/\sigma + 2r_c}. \qquad (8)$$

We could then use the Seebeck coefficient (S = 17 μV/K) and electrical conductivity (σ = 800 S/cm) of PEDOT/PSS to estimate of the maximum power density at a function of specific contact resistance r_c ($R_c = r_c/A$) at a given device thickness L (from 10 μm to 10 cm).
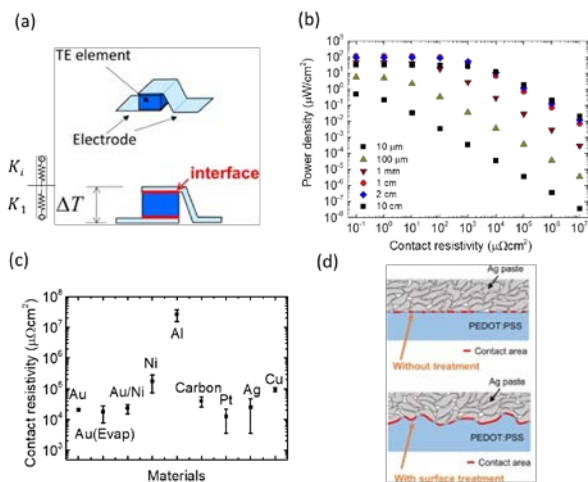

Figure 3. (a) Schematic of a one-leg conducting polymer thermoelectric module for evaluting the effect of contact resistance on thermoelectric performance. Reprinted with permission from [87]. Copyright 2018 Elsevier. (b) Calculated results on the power density of PEDOT/PSS thermoelectric module depending on the contact resistivity. (c) Contact resistivity between PEDOT/PSS and different metals. Reprinted with permission from [86]. Copyright 2017 Elsevier. (d) Schematic of the PEDOT:PS/Ag paste interface without and with surface treatment. Reprinted with permission from [87]. Copyright 2018 Elsevier.

Figure 3b shows that even with the same thermoelectric materials used, there were obvious orders of differences in the power output because of an increase in the contact resistivity. For a thin film device, the power density is normally reduced because of a small achievable temperature difference and high contact resistance; thus, a very low contact resistivity is required to raise their power density. For a device with a thickness of >1 mm, the power density gets saturated if the contact resistivity is <10^2 $\mu\Omega$cm^2. For example, a device with a thickness ~2 cm would show higher power density because of the balance between ΔT and internal resistance.

Previously, we used the transmission line method to measure the contact resistance between different types of metals and PEDOT/PSS films,[93] and observed orders of magnitude of differences in the contact resistivity between the materials. The metals with surface oxidation layers, including Ni, Al, and Cu, generally showed higher contact resistivity, which is reasonable because the surface oxide acted as a barrier for carrier transport from the metal to the conducting polymer to subsequently increase contact resistivity. The lowest contact resistivity between the metals and PEDOT/PSS was of the order of 10^4 $\mu\Omega$ cm^2, suggesting that the device performance was still strongly affected by contact resistance (Figure 3c). Note that

the power outputs of devices using PEDOT/PSS can be maximized using a thick (>1 cm) device. Therefore, the reported thermoelectric modules did not show an estimated power output in consideration of the material properties. In an inorganic TE system, r_c is typically <10^2 $\mu\Omega$ cm^2 because the soldering technique is established.

A surface treatment approach using ethylene glycol (EG) or Dimethyl sulfoxide (DMSO) on the electrode areas of the film could work to minimize the contact resistance,[94] primarily because of an increase in the contact area between PEDOT:PSS and Ag particles (Figure 3d). It is important to point out that reducing the carrier density in conducting polymers would mean an increased Seebeck coefficient and power factor; however, we could not successfully create a device with higher power output as the contact resistance depends on the carrier density in the polymers. A lower carrier density in conducting polymers may increase the barrier at the interface and result in higher contact resistivity. Quantitatively understand this trade-off relationship is underway.

4. Device Structure

4.1 Thermal gradient parallel to the substrate

To use the advantage of solution process organic materials, we could print these materials on certain substrates and attempt to connect them in parallel or series, and then apply the thermal gradient parallel to the substrate (Figure 4a). This structure is ideal to ease production. With this process, the in-plane thermoelectric properties of the materials determine the device performance, which corresponds to the typical characterization direction of the film samples. Thus, with a fixed temperature difference between the two sides of the substrate, the device performance could be compared with the material properties. On the one hand, this helps us understand the effect of contact resistance and thus optimize the fabrication process. On the other hand, in these devices, the substrates take up volume, indicating that the power density of these devices is not high.

In our previous study, we fabricated PEDOT:PSS thermoelectric modules on paper by screen printing (Figure 4b).[95] Here, the power output obtained for the large-area device was >50 μW at ΔT of ~100 K, which provided sufficient power to illuminate a light-emitting diode (LED). PEDOT/PSS showed remarkable thermal stability in the air, although the performance of the module decreased over time by the unstable interface between the silver paste and PEDOT:PSS. We demonstrated that organic
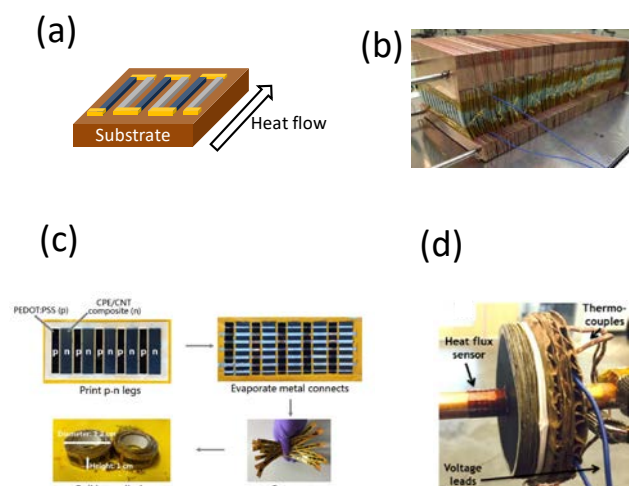

Figure 4. (a) Schematic of fin-type thermoelectric devices. Reprinted with permission from [86]. Copyright 2017 Elsevier. (b) Image of the PEDOT:PSS modules on paper sandwiched between copper plates. Reprinted with permission from [88]. Copyright 2014 The Royal Society of Chemistry. (c) Typical fabrication process for the rolled modules using PEDOT/PSS as p-type and CPE/CNT nanocomposite as n-type legs, respectively. Reprinted with permission from [89]. Copyright 2017 Wiley. (d) Radial TEG experimental setup consisting of 15 p–n couples stacked on a copper rod and cooled by natural convection. Reprinted with permission from [90]. Copyright 2017 Wiley.

thermoelectric modules could be used to harvest heat energy at low temperatures, although the stability of the interfaces must be improved.

Fang et al. reported the fabrication of organic thermoelectric modules on a Kapton substrate comprising >100 p- and n-legs (Figure 4c).[96] A rolled module design is normally used in the approach to easily maintain a temperature gradient along the substrate direction. The rolled modules produced a power output of 46 μW at a temperature difference of 65 K. Furthermore, Yee et. al used PEDOT/PSS and poly(nickel-1,1,2,2-ethenetetrathiolate) to fabricate a disk-like radial thermoelectric module on paper (Figure 4d).[97,98] Using this device, a hot pipe could be accommodated as the heat source; thus, active cooling was not required. The device produced an open-circuit voltage of 85 mV and a power density of 15 nW/cm^2 under a temperature difference of 45 K.

4.2 Thermal gradient vertical to the substrate

In inorganic thermoelectric devices, this structure is typical and could contain both p-leg and n-leg to make π-type devices or include only *p*-leg/*n*-leg and metal to produce the so-called uni-leg devices (Figure 5a).[99] Crispin et al. first reported a π-type thermoelectric module based on PEDOT/Tos and tetrathiafulvalene-tetracyanoquinodimethane (TTF-TCNQ).[32] The all-organic thermoelectric generator (TEG) device had 54 legs with lengths of 40 μm and was fabricated within a pre-patterned epoxy-based polymer cavity. It yielded a maximum power output of 0.128 μW at a temperature difference of 10 K (Figure 5b). Sondergaard et al. demonstrated the large-scale fabrication of a uni-leg thermoelectric module using roll-to-roll printing technologies, which they claimed to be capable of >10,000 serial connections (Figure 5c). [100]

Suemori et al. used a printing process to fabricate a 150-μm-thick flexible thermoelectric generator on a polyethylene naphthalate film substrate (Figure 5d),[101] where the composite material was composed of carbon nanotubes and polystyrene. Consisting of 1985 individual devices, the TEG generated ~5.5 μW/cm^2 of power at a temperature difference of 70°C. Nonoguchi et al. reported a π-type 12-cm scale generator
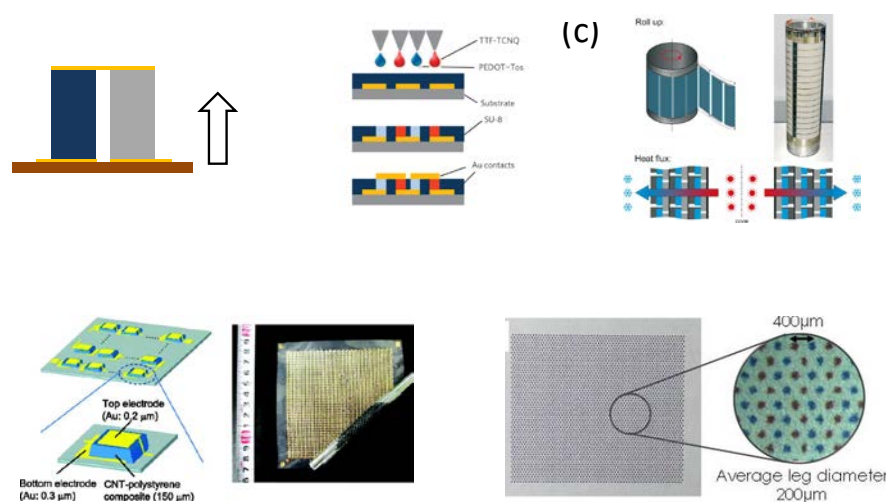

Figure 5. (a) Schematic of π-type thermoelectric devices. Reprinted with permission from [86]. Copyright 2017 Elsevier. (b) The printed organic thermoelectric devices reported by Bubnova et al. [32] Copyright 2011 Springer. (c) The thermoelectric device fabricated with the roll-to-roll process. Reprinted by permission from [93] Copyright 2013 Wiley. (d) Schematic and image of thermoelectric modules composed of 1985 individual thermoelectric devices, each being 1.5 mm wide, 0.8 mm long, and 0.15 mm thick, connected in series on a polyethylene naphthalate film substrate. Reprinted by permission from [94] Copyright 2013 American Institute of Physics. (e) 3600 legs are printed in an area of 36.0 mm by 31.2 mm on a conventional copy paper to show a large fill factor. Reprinted by permission from [96] Copyright 2017 American Institute of Physics.

providing thermoelectric outputs high enough to drive an LED.[102] Yee et al. suggested organic thermoelectric devices exhibiting an excellent performance by positioning *n*- and *p*-type legs in a closed-packed hexagonal layout[103]. The concept can be performed using paper as a substrate, but roll-to-roll printing techniques are applicable (Figure 5e).

Although such a thermal gradient structure is demonstrated in the field of inorganic thermoelectrics, directly applying it to organic thermoelectric materials can be difficult because of several reasons. The first is the film thickness.[104,105] A constant temperature gradient in π-type devices can be achieved with a film thickness of typically a millimeter scale, which is a challenging task in solution processing. The second is the
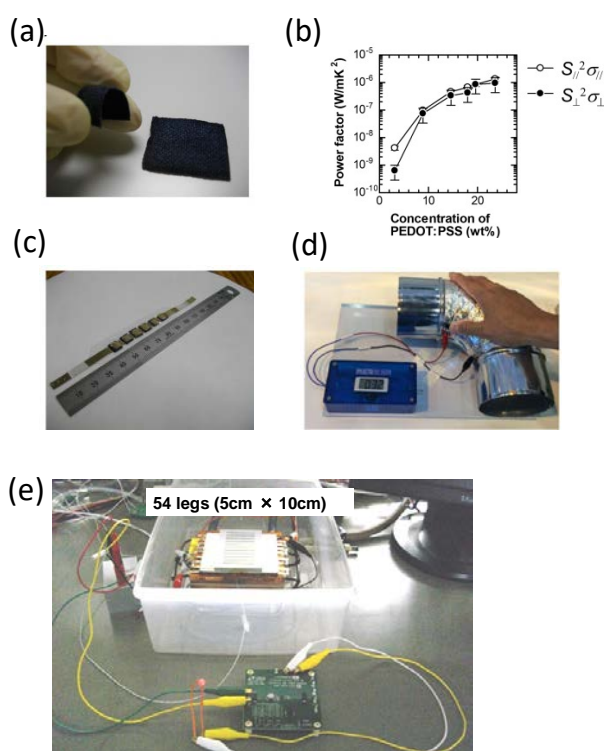

Figure 6. (a) Image of thePEDOT:PSS/fabric composite element. (b) Power factor of the fabric composite element as a function of PEDOT:PSS concentration. (c) Image of the fabric module based on PEDOT:PSS/fabric composite. (d) Image of the fabric module on piping. (e) Image of the setup for thermoelectric power generation and LED operation by the fabric modules. Reprinted by permission from [101] Copyright 2017 Elsevier.

anisotropy of film samples. For a film sample, it is easy to measure and compare the in-plane Seebeck coefficient and electrical conductivity; however, extracting the through-plane quantities is not straightforward. In π-type devices, the through-plane thermoelectric properties of the materials largely determine the device performance. As reported in our previous work, the through-plane thermoelectric properties are lower than the in-plane properties.[27,106,107]

These issues may be overcome by considering the fabrication and transport properties of nonwoven fabric-composite thermoelectric elements via impregnation with the

polymer PEDOT/PSS (Figure 6a).[108] Here, a high thermal resistance was attributed to the porous structure formed in the fabric after the solvent evaporation of the PEDOT/PSS solution. Moreover, the polymer films covering the surface of the fibers in the fabric connected the fibers to form electrical conduction paths, yielding isotropic electrical conductivity at high PEDOT/PSS concentrations (Figure 6b). These two factors provided the optimum PEDOT/PSS concentration for the power density per PEDOT/PSS content. Note that optimizing the power density per polymer content could contribute to the inexpensive fabrication of thermoelectric modules from conducting polymers (Figure 6c). Furthermore, such a flexible device can be bounded on the piping surface to harvest energy from the fluid within the piping (Figure 6d). The flexible thermoelectric module fabricated from the nonwoven fabric-composite achieved a power output sufficient to power an LED (Figure 6e). Contact electrical resistance at the polymer-electrode junctions was significantly reduced as the contact area widened because of the wavy surface of the fabric composite. Indeed, this approach provides a new method for making isotropic conducting samples from anisotropic materials.

4.3 Substrate-free devices

As discussed in the previous section, printing organic materials on substrates is a straightforward approach to fabricate devices. However, as the substrates take up volume, the power density of these devices would not be high. The substrate volume can be minimized with organic thermoelectric modules by laminating free-standing PEDOT/PSS films, polyimide, and Ni foil (Figure 7).[93,109]
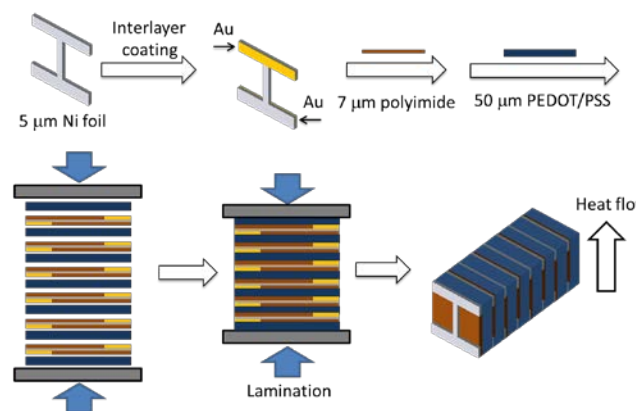

Figure 7. Schematic of the thermal lamination process used to fabricate the polymer thermoelectric devices. The Ni foil was cut into a square and modified into an I-shape. Edges on both sides were coated with 20 nm of Au. The as-prepared Ni foils, polyimide films, and freestanding PEDOT/PSS films were stacked within a mold for alignment and laminated at 100°C. Reprinted by permission from [102] Copyright 2019 American Chemical Society.

In Section 3, we reported that a thick device (with a thickness of ~2 cm) is necessary to maximize the power density using PEDOT/PSS, primarily because of a relatively high contact resistivity at the interface. Here we fixed the device height at

2.2 cm according to the commercial availability of the precision film cutter (NOGAMIGIKEN Co., Ltd.).

Accordingly, the thicknesses of the PEDOT/PSS film, the polyimide film, and the Ni foil were fixed at 50, 7, and 5 μm. The 5-μm-thick Ni foil and 7-μm-thick polyimide film are the minimum thicknesses commercially applicable. The PEDOT/PSS film was imparted with high electrical conductivity by adding the high boiling point solvent ethylene glycol, improving the crystallinity and ordering of PEDOT nanocrystals during film formation. An increase in the thickness of the PEDOT/PSS film decreased the order of the PEDOT nanocrystals, resulting in lower electrical conductivity.

A relatively large contact area between PEDOT/PSS and Ni was required for the high contact resistance between the metals and the conducting polymers. Furthermore, it was necessary to consider the heat lost at the contact area. To match the thermal resistance between Ni and PEDOT/PSS and improve the device performance, we reduced the volume of Ni by altering the shape of the Ni foil into an I-shape (Figure 8a) while the width and height of the device was fixed at 22 mm. We calculated the device efficiency by altering the contact area between PEDOT/PSS and Ni (a), as well as the width of the Ni foil (b). As shown in Figure 8b, the effective thermal resistance $1/\kappa_c$ of the contact area between PEDOT/PSS and Ni on both
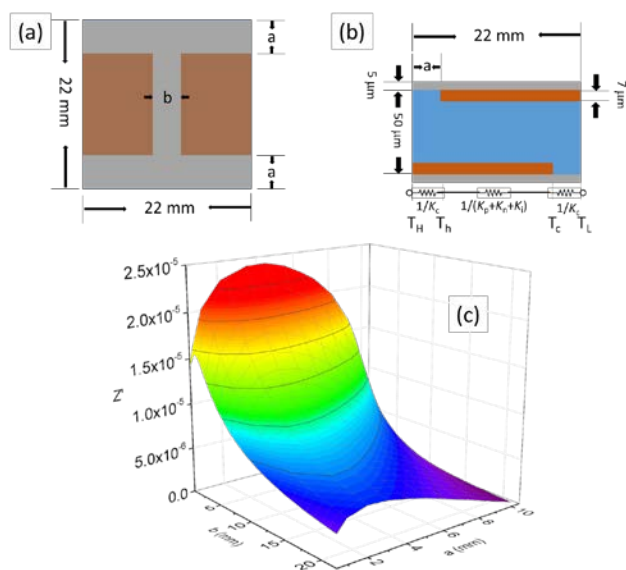

Figure 8. (a) Schematic of an I-shaped Ni foil. (b) Structure and thermal resistor network of a thermoelectric module using I-shaped Ni foils. (c) Calculated value of Z' as a function of a and b. Reprinted by permission from [102] Copyright 2019 American Chemical Society.

sides, and the thermal resistance of the active area $1/(\kappa_p + \kappa_n + \kappa_i)$ were assumed to be connected in series.

Considering one p–n pair, the device efficiency was approximately

$$\eta \approx \frac{1}{4} \cdot \frac{(S_p - S_n)^2}{(R_p + R_n + R_c)(K_p + K_n + K_i)} \cdot \frac{K_c}{K_c + 2(K_p + K_n + K_i)} \times \Delta T. \quad (9)$$

Here, we define Z' as follows:

$$Z' = \frac{(S_p - S_n)^2}{(R_p + R_n + R_c)(K_p + K_n + K_i)} \cdot \frac{K_c}{K_c + 2(K_p + K_n + K_i)}, \quad (10)$$

where S is the Seebeck coefficient, R is the electrical resistance, and K is the thermal conductance, with the subscripts p and n denoting the p-type and n-type materials. R_c and K_i are the corresponding contact resistance and thermal loss from the insulation layer. The values of Z' could be maximized to obtain the best thermoelectric device performance, as shown by the calculation results in Figure 8c. Z' increased as b significantly decreased, which could be attributed to a decrease in the thermal conductance of Ni. The optimum value of b was ~2 mm, while b values of <2 mm resulted in increased electrical resistance and thus low Z'. The optimal value of a was ~3 mm, although the changes in Z' as a varied from 2 to 4 mm were not significant. When a decreased to <1 mm, the contact resistance between PEDOT/PSS and Au–Ni significantly increased, whereas a exceeding 5 mm resulted in a low intrinsic temperature
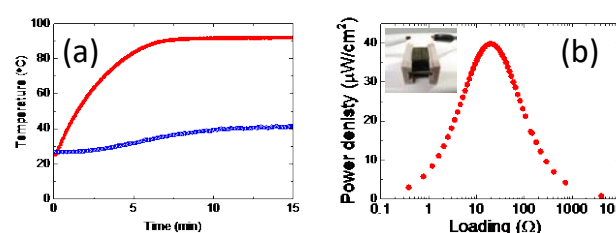

Figure 9. (a) Temperatures at the hot sides (red) and cold sides (blue) of the devices fabricated using I-shaped Ni foil. (b) Power output of the devices on a hot plate at 100 °C without heat sink at a stable state. The inset is a photograph of the module. Reprinted by permission from [102] Copyright 2019 American Chemical Society.

difference. Both caused Z' to significantly decrease.

The thermoelectric device was fabricated with a = b = ~2 mm. At a hot source temperature of 100°C, it achieved a stable temperature difference of 50 K under natural cooling conditions without any heat sink (Figure 9a). Its corresponding power density was as high as 40 μW/cm² (Figure 9b). In our laboratory, a typical area for the device is ~5 cm², which contains ~300 legs. The average weight of the device was only 10 g, which indicates that it could continuously deliver 0.2 mW for practical applications.

4.4 Flexible devices considering anisotropicity

Anisotropicity in the materials is considered while fabricating flexible devices such that the heat flow is transferred from a vertical direction to a horizontal direction (Figure 10a). This concept is known in the field of inorganic thermoelectrics but is not generally applied in organic materials. Takeda et al. reported the fabrication of inorganic thermoelectric devices on a flexible substrate composed of polyimide and copper sheets.[110,111] The flexible substrate was formed of high and low thermal conductivity materials. When the device was placed on a hot source, the vertical heat flow transferred to a horizontal direction. Experimentally, they confirmed that the temperature difference (ΔT_{out}) applied between the outer surfaces of the

device could transfer to an in-plane temperature difference (ΔT_{in}), measured at 16.7 K when ΔT_{out} was 57.8 K, which is consistent with the values obtained using the finite element method.[111]

Fujifilm featured a similar in-plane configuration using p-type CNT with a flexible single-leg type thermoelectric module
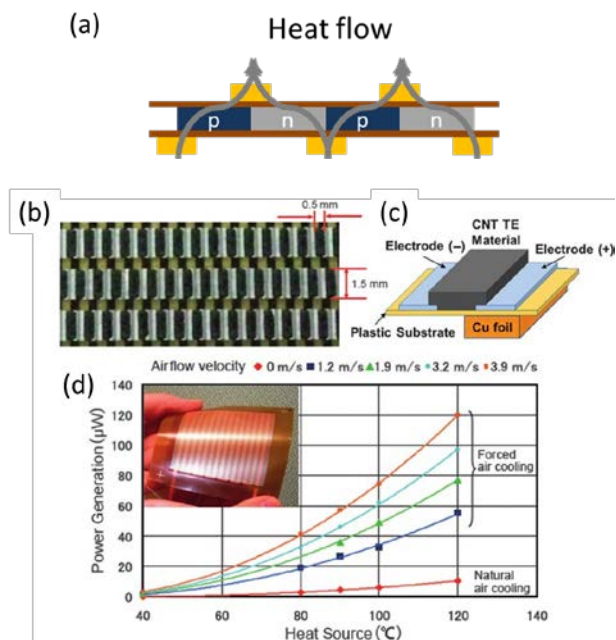

Figure 10. (a) Schematic of a flexible device transfering the heat flow from a vertical direction to a horizontal direction. Configuration and power output of a carbon nanotube (CNT)-based thermoelectric (TE) module fabricated by Fujifilm Corporation. (b) Image of a CNT-based TE pattern fabricated by stencil printing, and (c) a schematic of a single leg in the pattern. (d) The generated power output at different airflow rates. The inset shows a photograph of the TE module consisting of p-type CNT-based composite material. The TE module can achieve a maximum power output of 120 μW when the hot side is 120°C and the flow rate of the cool air is 3.9 m/s. Reprinted by permission from [105] Copyright 2018 Materials Research Society.

(10×10 cm^2) (Figure 10b-c)[112]. The thermoelectric module was mounted onto an Al fin with flowing air for cooling, and then the heat was extracted from a hot pipe with a diameter of 80 mm. The power output was measured at different airflow rates in the range of 0–3.9 m/s. Based on the results, the module generated a power output of 10 μW by natural air cooling when the hot-side temperature was 120°C, but could remarkably increase to 50 and 120 μW when the airflow rate was 1.2 and 3.9 m/s, respectively.

Because organic materials generally have a lower in-plane thermal conductivity than inorganic semiconductors and CNT, a larger ΔT_{in} could be expected when using a similar design.[106] The fabrication of a flexible device using PEDOT/PSS and electroplating Ni film is currently a much-researched topic.

5. DC-to-DC converter and self-powered sensors

Commercial sensors operate at a typical voltage of several volts, but thermoelectric devices cannot provide a high open-circuit

voltage (tens of mV to hundreds of mV). Thus, a DC-to-DC converter is necessary to fabricate self-powered sensors.[113]
There are different types of DC-to-DC converters commercially available. One important parameter when evaluating a DC-to-DC converter is the minimum input voltage required to operate the converter. LTC3108 (Linear Technology) is extensively used in inorganic thermoelectric modules,[114] because it could use a voltage as low as 20 mV, which is achievable for many inorganic thermoelectric modules; however, this converter requires a low internal resistance. Our experimental results for operating this converter with different thermoelectric devices and thermoelectrochemical devices are shown in Table 1. For the device with an internal resistance of 1.5 Ω, we could drive the converter with an open-circuit voltage of ~33 mV. If the internal resistance increased to 10 Ω, a higher open-circuit voltage of 70 mV was required. For a device with an internal resistance of 150 Ω, an open-circuit voltage of 450 mV was required to boost the charge pump. From the datasheet, a milliampere scale current was required to boost LTC3108, which is about the same as our

Table 1. Experimental results on the relationship of the open-circuit voltage and internal resistance of the thermoelectric devices that could boost the converter

Type of converter	Open-circuit voltage (mV)	Internal resistance (Ω)
LTC3108	33	1.5
	70	10
	90	20
	125	30
	165	50
	210	70
	270	80
	370	110
	420	140
	450	150
AP4470	280	100
	400	1000
	500	10000

measurement results. Another DC-to-DC converter we have tested was AP4470 (Asahi Kasei Microdevices). It could only be driven with an open-circuit voltage of >200 mV but needs a small current. Based on our experiment results with organic thermoelectric devices, we could start to boost AP4470 even when the internal resistance was more significant than 10000 Ω if the open-circuit voltage could achieve 500 mV.

For the organic thermoelectric devices, it was not easy to achieve low internal resistance because of the limitation of film thickness, the relatively low electrical conductivity of organic materials, and the relatively high contact resistance. Thus, we
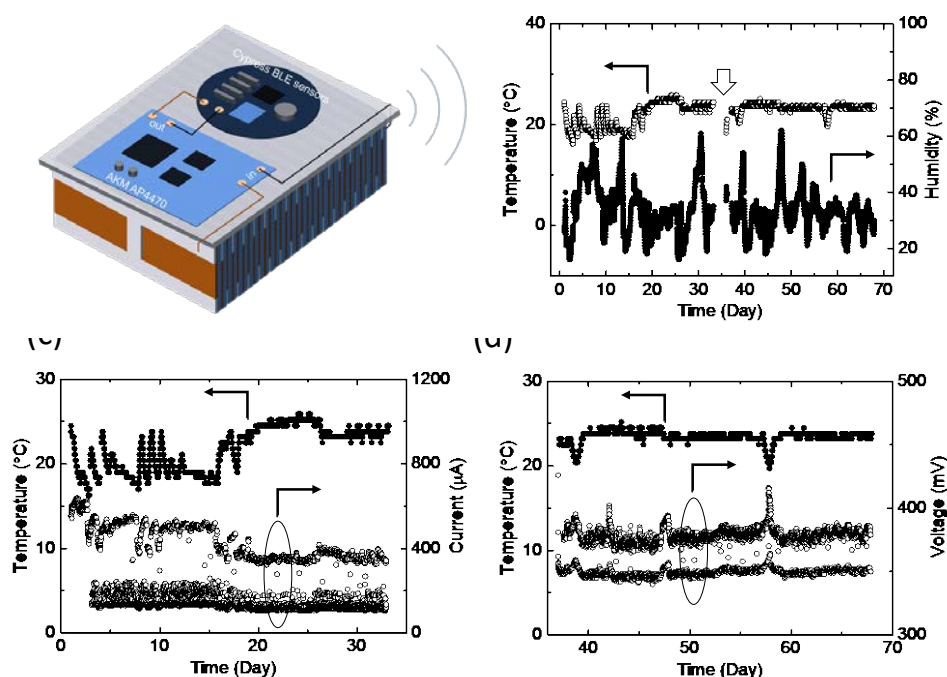
Figure 11. (a) A schematic of the self-powered sensor combining a laminated device with AP4470 and cypress BLE sensors. (b) Humidity and temperature changes recorded by self-powered sensors. The current (c) and voltage (d) on AP4470.

fabricated the self-powered sensors by combining the laminated device with AP4470 and cypress BLE sensor (Figure 11a). As the cypress BLE sensor is initially designed for solar cells, we removed the solar cells and implemented them with the DC-to-DC converter. The size of the organic thermoelectric module was ~2.2 ×5 ×2.2 cm^3. On a 100°C hot source, the module delivered ~0.2 mW to boost the DC-to-DC converter. Note that the maximum power output from the module was ~0.4 mW at the optimal load.

The self-powered sensor transferred the humidity and temperature signal to a tablet, PC, or smartphone every 5 s to 10 min. We monitored the humidity and temperature in the lab for over 70 days (the hot side temperature is fixed at 100°C all the time), and recorded corresponding changes during the day and the night. The temperature in the room stabilized after we have turned on the air conditioner in the room (Figure 11b).

We measured both the current (Figure 11c) and voltage (Figure 11d) on the DC-to-DC converter with time and observed two characteristics of the voltage and current change. Firstly, the thermoelectric module delivered more power when the room temperature was reduced practically because a more significant temperature difference was achieved inside the device. Secondly, the BLE sensor/DC-to-DC showed some tendency to switch off when no more power was required; therefore, there was a reversed change of the current and voltage on the converters. It is essential to report that no significant degeneration of both the voltage and current occurred in the 70 days, even without encapsulation of the devices. Note that the stability test terminated because of

Covid-19, although much longer life could be expected. Our previous studies showed that the performance of the printed module decreased over time, which was attributed to the unstable interface between the silver paste and PEDOT/PSS. Here, we reported that selecting the right interface material could significantly increase the stability of the devices. Moreover, we tested other modules fabricated one year ago and observed no significant difference in the power output compared to the freshly prepared ones. We are confident that the organic thermoelectric module could show excellent stability that is even comparable to that of inorganic thermoelectric materials.

6. Conclusion

This study summarized recent efforts concerning the fabrication of organic thermoelectric devices. We demonstrated that the thermoelectric performance for organic semiconductors is still lesser than their inorganic counterparts; however, the devices could achieve respective power output through device engineering. Furthermore, the organic thermoelectric devices possess other advantages such as being lightweight. For instance, a device containing ~300 legs weighs only 10 g, which indicates that it could continuously deliver power of 0.2 mW at a hot-side temperature of 100°C under natural cooling without a heat sink. The stability issue is another concern for the practical application of organic thermoelectric modules because energy harvesting devices face competition with batteries, which are known to have high energy density and lifetime. We demonstrated that a self-powered sensor based on

an organic thermoelectric module could show excellent stability over 70 days under a continuous working condition. No significant performance degeneration was observed during the period, and even no encapsulation was applied to the devices. This result is encouraging; thus, we suggest that organic thermoelectric materials could be an ideal candidate for energy harvesting and fabrication of self-powered sensors. Using newly developed organic conducting materials, we can only expect thermoelectric devices with high added value.

Conflicts of interest

There are no conflicts to declare.

Acknowledgements

References

1   A. Al-Fuqaha, M. Guizani, M. Mohammadi, M. Aledhari and M. Ayyash, *IEEE Commun. Surv. TUTORIALS*, 2015, **17**, 2347–2376.

2   R. J. M. Vullers, R. van Schaijk, I. Doms, C. Van Hoof and R. Mertens, *Solid. State. Electron.*, 2009, **53**, 684–693.

3   C. K. Ho and R. Zhang, *IEEE Trans. Signal Process.*, 2012, **60**, 4808–4818.

4   S. Ulukus, A. Yener, E. Erkip, O. Simeone, M. Zorzi, P. Grover and K. Huang, *IEEE J. Sel. Areas Commun.*, 2015, **33**, 360–381.

5   A. Harb, *Renew. Energy*, 2011, **36**, 2641–2654.

6   N. S. Hudak and G. G. Amatucci, *J. Appl. Phys.*, 2008, **103**, 101301.

7   B. Russ, A. Glaudell, J. J. Urban, M. L. Chabinyc and R. A. Segalman, *Nat. Rev. Mater.*, 2016, **1**, 16050.

8   G. J. Snyder, in *ENERGY HARVESTING TECHNOLOGIES*, ed. Priya, S and Inman, DJ, 2009, pp. 325–336.

9   G. J. Snyder and E. S. Toberer, *Nat. Mater.*, 2008, **7**, 105–114.

10   B. Poudel, Q. Hao, Y. Ma, Y. Lan, A. Minnich, B. Yu, X. Yan, D. Wang, A. Muto, D. Vashaee, X. Chen, J. Liu, M. S. Dresselhaus, G. Chen and Z. Ren, *Science*, 2008, **320**, 634–638.

11   M. S. Dresselhaus, G. Chen, M. Y. Tang, R. Yang, H. Lee, D. Wang, Z. Ren, J.-P. Fleurial and P. Gogna, *Adv. Mater.*, 2007, **19**, 1043–1053.

12   J. P. Heremans, V. Jovovic, E. S. Toberer, A. Saramat, K. Kurosaki, A. Charoenphakdee, S. Yamanaka and G. J. Snyder, *Science*, 2008, **321**, 554–557.

13   J. R. Sootsman, D. Y. Chung and M. G. Kanatzidis, *Angew. CHEMIE-INTERNATIONAL Ed.*, 2009, **48**, 8616–8639.

14   G. Tan, L.-D. Zhao and M. G. Kanatzidis, *Chem. Rev.*, 2016, **116**, 12123–12149.

15   J.-F. Li, W.-S. Liu, L.-D. Zhao and M. Zhou, *NPG ASIA Mater.*, 2010, **2**, 152–158.

16   Q. Zhang, Y. Sun, W. Xu and D. Zhu, *Adv. Mater.*, 2014, **26**, 6829–6851.

17   D. Venkateshvaran, M. Nikolka, A. Sadhanala, V. Lemaur, M. Zelazny, M. Kepa, M. Hurhangee, A. J. Kronemeijer, V. Pecunia, I. Nasrallah, I. Romanov, K. Broch, I. McCulloch, D. Emin, Y. Olivier, J. Cornil, D. Beljonne and H. Sirringhaus, *Nature*, 2014, **515**, 384–388.

18   O. Bubnova and X. Crispin, *ENERGY Environ. Sci.*, 2012, **5**, 9345–9362.

19   Y. Du, S. Z. Shen, K. Cai and P. S. Casey, *Prog. Polym. Sci.*, 2012, **37**, 820–841.

20   Q. Wei, M. Mukaida, K. Kirihara, Y. Naitoh and T. Ishida, *Materials*, 2015, **8**, 732–750.

21   M. Culebras, C. M. Gomez and A. Cantarero, *Materials*, 2014, **7**, 6701–6732.

22   Y. Chen, Y. Zhao and Z. Liang, *ENERGY Environ. Sci.*, 2015, **8**, 401–422.

23   N. Dubey and M. Leclerc, *J. Polym. Sci. Part B Polym. Phys.*, 2011, **49**, 467–475.

24   M. He, F. Qiu and Z. Lin, *Energy Environ. Sci.*, 2013, **6**, 1352–1361.

25   N. Toshima, *Synth. Met.*, 2017, **225**, 3–21.

26   M.-K. Han, Y. Jin, D.-H. Lee and S.-J. Kim, *Materials*, 2017, **10**, 1235.

27   Q. Wei, M. Mukaida, K. Kirihara and T. Ishida, *ACS Macro Lett.*, 2014, **3**, 948–952.

28   P. E. FIELDING and F. GUTMAN, *J. Chem. Phys.*, 1957, **26**, 411–419.

29   N. Kim, S. Lienemann, I. Petsagkourakis, D. A. Mengistie, S. Kee, T. Ederth, V. Gueskine, P. Leclere, R. Lazzaroni, X. Crispin and K. Tybrandt, *Nat. Commun.*, 2020, **11**, 1424.

30   Y. Chen, M. He, J. Tang, G. C. Bazan and Z. Liang, *Adv. Electron. Mater.*, 2018, **4**, 1800200.

31   G.-H. Kim, L. Shao, K. Zhang and K. P. Pipe, *Nat. Mater.*, 2013, **12**, 719–723.

32   O. Bubnova, Z. U. Khan, A. Malti, S. Braun, M. Fahlman, M. Berggren and X. Crispin, *Nat. Mater.*, 2011, **10**, 429–433.

33   Q. Wei, M. Mukaida, K. Kirihara, Y. Naitoh and T. Ishida, *Appl. Phys. EXPRESS*, 2014, **7**, 031601.

34   Y. Ichinose, A. Yoshida, K. Horiuchi, K. Fukuhara, N. Komatsu, W. Gao, Y. Yomogida, M. Matsubara, T. Yamamoto, J. Kono and K. Yanagi, *Nano Lett.*, 2019, **19**, 7370–7376.

35   K. Harada, M. Sumino, C. Adachi, S. Tanaka and K. Miyazaki, *Appl. Phys. Lett.*, 2010, **96**, 253304.

36   W. Shi, T. Deng, G. Wu, K. Hippalgaonkar, J.-S. Wang and S.-W. Yang, *Adv. Mater.*, 2019, **31**, 1901956.

37   J. J. Urban, A. K. Menon, Z. Tian, A. Jain and K. Hippalgaonkar, *J. Appl. Phys.*, 2019, **125**, 180902.

38   C. Cho, B. Stevens, J.-H. Hsu, R. Bureau, D. A. Hagen, O. Regev, C. Yu and J. C. Grunlan, *Adv. Mater.*, 2015, **27**, 2996–3001.

39   J. Liu, L. Qiu, G. Portale, M. Koopmans, G. ten Brink, J. C. Hummelen and L. J. A. Koster, *Adv. Mater.*, 2017, **29**, 1701641.

40   C. Wan, X. Gu, F. Dang, T. Itoh, Y. Wang, H. Sasaki, M. Kondo, K. Koga, K. Yabuki, G. J. Snyder, R. Yang and K. Koumoto, *Nat. Mater.*, 2015, **14**, 622–627.

41   C. Cho, M. Culebras, K. L. Wallace, Y. Song, K. Holder, J.-H. Hsu, C. Yu and J. C. Grunlan, *NANO ENERGY*, 2016, **28**, 426–432.

42   J. Liu, M. P. Garman, J. Dong, B. van der Zee, L. Qiu, G. Portale, J. C. Hummelen and L. J. A. Koster, *ACS Appl. ENERGY Mater.*, 2019, **2**, 6664–6671.

43   J. Liu, G. Ye, B. van der Zee, J. Dong, X. Qiu, Y. Liu, G. Portale, R. C. Chiechi and L. J. A. Koster, *Adv. Mater.*, 2018, **30**, 1804290.

44   B. Russ, M. J. Robb, F. G. Brunetti, P. L. Miller, E. E. Perry, S. N. Patel, V. Ho, W. B. Chang, J. J. Urban, M. L. Chabinyc, C. J. Hawker and R. A. Segalman, *Adv. Mater.*, 2014, **26**, 3473–3477.

45   B. Doerling, J. D. Ryan, J. D. Craddock, A. Sorrentino, A. El Basaty, A. Gomez, M. Garriga, E. Pereiro, J. E. Anthony, M. C. Weisenberger, A. R. Goni, C. Muller and M. Campoy-Quiles, *Adv. Mater.*, 2016, **28**, 2782–2789.

46   D. Madan, X. Zhao, R. M. Ireland, D. Xiao and H. E. Katz, *APL Mater.*, 2017, **5**, 086106.

47   Y. Lu, Z.-D. Yu, Y. Liu, Y.-F. Ding, C.-Y. Yang, Z.-F. Yao, Z.-Y. Wang, H.-Y. You, X.-F. Cheng, B. Tang, J.-Y. Wang and J. Pei, *J. Am. Chem. Soc.*, 2020, **142**, 15340–15348.

48   C. Y. Yang, Y. F. Ding, D. Huang, J. Wang, Z. F. Yao, C. X. Huang, Y. Lu, H. I. Un, F. D. Zhuang, J. H. Dou, C. an Di, D. Zhu, J. Y. Wang, T. Lei and J. Pei, *Nat. Commun.*, 2020, **11**, 3292.

49   D. Yuan, D. Huang, S. M. Rivero, A. Carreras, C. Zhang, Y. Zou, X. Jiao, C. R. McNeill, X. Zhu, C. an Di, D. Zhu, D. Casanova and J. Casado, *Chem*, 2019, **5**, 964-976.

50   Y. Nonoguchi, K. Ohashi, R. Kanazawa, K. Ashiba, K. Hata, T. Nakagawa, C. Adachi, T. Tanase and T. Kawai, *Sci. Rep.*, 2013, **3**, 3344.

51   G. Zuo, Z. Li, E. Wang and M. Kemerink, *Adv. Electron. Mater.*, 2018, **4**, 1700501.

52   K. Shi, F. Zhang, C.-A. Di, T.-W. Yan, Y. Zou, X. Zhou, D. Zhu, J.-Y. Wang and J. Pei, *J. Am. Chem. Soc.*, 2015, **137**, 6979–6982.

53   X. Zhao, D. Madan, Y. Cheng, J. Zhou, H. Li, S. M. Thon, A. E. Bragg, M. E. DeCoster, P. E. Hopkins and H. E. Katz, *Adv. Mater.*, 2017, **29**, 1606928.

54   A. K. Menon, R. M. W. Wolfe, S. Kommandur and S. K. Yee, *Adv. Electron. Mater.*, 2019, **5**, 1800884.

55   R. Tian, C. Wan, Y. Wang, Q. Wei, T. Ishida, A. Yamamoto, A. Tsuruta, W. Shin, S. Li and K. Koumoto, *J. Mater. Chem. A*, 2017, **5**, 564–570.

56   D. Kiefer, A. Giovannitti, H. Sun, T. Biskup, A. Hofmann, M. Koopmans, C. Cendra, S. Weber, L. J. A. Koster, E. Olsson, J. Rivnay, S. Fabiano, I. McCulloch and C. Muller, *ACS ENERGY Lett.*, 2018, **3**, 278–285.

57   Y. Xia, K. Sun and J. Ouyang, *Adv. Mater.*, 2012, **24**, 2436–2440.

58   K. Sun, S. Zhang, P. Li, Y. Xia, X. Zhang, D. Du, F. H. Isikgor and J. Ouyang, *J. Mater. Sci. Electron.*, 2015, **26**, 4438–4462.

59   H. Yano, K. Kudo, K. Marumo and H. Okuzaki, *Sci. Adv.*, 2019, **5**, eaav9492.

60   X. Wang, X. Zhang, L. Sun, D. Lee, S. Lee, M. Wang, J. Zhao, Y. Shao-Horn, M. Dinc\u a, T. Palacios and K. K. Gleason, *Sci. Adv.*, 2018, **4**, eaat5780.

61   B. Cho, K. S. Park, J. Baek, H. S. Oh, Y.-E. K. Lee and M. M. Sung, *NANO Lett.*, 2014, **14**, 3321–3327.

62   M. Mueller, M. Fabretto, D. Evans, P. Hojati-Talemi, C. Gruber and P. Murphy, *Polymer*, 2012, **53**, 2146–2151.

63   Q. Wei, Y. Sugihara, T. Tanabe, M. Mukaida, K. Kirihara, Y. Naitoh and T. Ishida, *Polymer*, 2015, **66**, 38–42.

64   S. He, M. Mukaida, K. Kirihara, L. Lyu and Q. Wei, *Polymers*, 2018, **10**, 1065.

65   Z. Fan and J. Ouyang, *Adv. Electron. Mater.*, 2019, **5**, 1800769.

66   I. Salzmann, G. Heimel, M. Oehzelt, S. Winkler and N. Koch, *Acc. Chem. Res.*, 2016, **49**, 370–378.

67   B. Luessem, M. Riede and K. Leo, *Phys. STATUS SOLIDI A-APPLICATIONS Mater. Sci.*, 2013, **210**, 9–43.

68   N. Massonnet, A. Carella, A. de Geyer, J. Faure-Vincent and J.-P. Simonato, *Chem. Sci.*, 2015, **6**, 412–417.

69   M. N. Gueye, A. Carella, N. Massonnet, E. Yvenou, S. Brenet, J. Faure-Vincent, S. Pouget, F. Rieutord, H. Okuno, A. Benayad, R. Demadrille and J.-P. Simonato, *Chem. Mater.*, 2016, **28**, 3462–3468.

70   L. Lyu, K. Kirihara, Y. Okigawa, M. Hasegawa, W. Ding, Y. Wang, M. Mukaida, Y. Zhou and Q. Wei, *Org. Electron.*, 2020, **78**, 105615.

71   Q. Wei, M. Mukaida and T. Ishida, *J. Phys. Chem. C*, 2018, **122**, 15922–15928.

72   N. Massonnet, A. Carella, O. Jaudouin, P. Rannou, G. Laval, C. Celle and J.-P. Simonato, *J. Mater. Chem. C*, 2014, **2**, 1278–1283.

73   M. Culebras, C. M. Gomez and A. Cantarero, *J. Mater. Chem. A*, 2014, **2**, 10109–10115.

74   Z. U. Khan, J. Edberg, M. M. Hamedi, R. Gabrielsson, H. Granberg, L. Wagberg, I. Engquist, M. Berggren and X. Crispin, *Adv. Mater.*, 2016, **28**, 4556–4562.

75   Q. Wei, M. Mukaida, K. Kirihara, Y. Naitoh and T. Ishida, *ACS Appl. Mater. Interfaces*, 2016, **8**, 2054–2060.

76   J. Hynynen, D. Kiefer and C. Muller, *RSC Adv.*, 2018, **8**, 1593–1599.

77   D. Kiefer, L. Yu, E. Fransson, A. Gomez, D. Primetzhofer, A. Amassian, M. Campoy-Quiles and C. Muller, *Adv. Sci.*, 2017, **4**, 1600203.

78   O. Zapata-Arteaga, B. Dörling, A. Perevedentsev, J. Martín, J. S. Reparaz and M. Campoy-Quiles, *Macromolecules*, 2020, **53**, 609–620.

79   H. Li, M. E. DeCoster, C. Ming, M. Wang, Y. Chen, P. E. Hopkins, L. Chen and H. E. Katz, *Macromolecules*, 2019, **52**, 9804–9812.

80   H. Li, M. E. DeCoster, R. M. Ireland, J. Song, P. E. Hopkins and H. E. Katz, *J. Am. Chem. Soc.*, 2017, **139**, 11149–11157.

81   R. Fujimoto, Y. Yamashita, S. Kumagai, J. Tsurumi, A. Hinderhofer, K. Broch, F. Schreiber, S. Watanabe and J. Takeya, *J. Mater. Chem. C*, 2017, **5**, 12023–12030.

82   Y. Yamashita, J. Tsurumi, M. Ohno, R. Fujimoto, S. Kumagai, T. Kurosawa, T. Okamoto, J. Takeya and S. Watanabe, *Nature*, 2019, **572**, 634–638.

83   K. Kang, S. Watanabe, K. Broch, A. Sepe, A. Brown, I. Nasrallah, M. Nikolka, Z. Fei, M. Heeney, D. Matsumoto, K. Marumoto, H. Tanaka, S. Kuroda and H. Sirringhaus, *Nat. Mater.*, 2016, **15**, 896.

84   K. Kang, S. Schott, D. Venkateshvaran, K. Broch, G. Schweicher, D. Harkin, C. Jellett, C. B. Nielsen, I. McCulloch and H. Sirringhaus, *Mater. Today Phys.*, 2019, **8**, 112–122.

85   S. N. Patel, A. M. Glaudell, K. A. Peterson, E. M. Thomas, K. A. O'Hara, E. Lim and M. L. Chabinyc, *Sci. Adv.*, 2017, **3**, e1700434.

86   S. N. Patel, A. M. Glaudell, D. Kiefer and M. L. Chabinyc, *ACS Macro Lett.*, 2016, **5**, 268–272.

87   A. M. Glaudell, J. E. Cochran, S. N. Patel and M. L. Chabinyc, *Adv. ENERGY Mater.*, 2015, **5**, 1401072.

88   K. C. See, J. P. Feser, C. E. Chen, A. Majumdar, J. J. Urban and R. A. Segalman, *Nano Lett.*, 2010, **10**, 4664–4667.

89   Y. Wang, K. Cai and X. Yao, *ACS Appl. Mater. Interfaces*, 2011, **3**, 1163–1166.

90   B. Zhang, J. Sun, H. E. Katz, F. Fang and R. L. Opila, *ACS Appl. Mater. Interfaces*, 2010, **2**, 3170–3178.

91   G. O. Park, J. W. Roh, J. Kim, K. Y. Lee, B. Jang, K. H. Lee and W. Lee, *Thin Solid Films*, 2014, **566**, 14–18.

92   Ir. Hugo S.L.C. Hens, in *Building Physics - Heat, Air and Moisture*, John Wiley & Sons, Ltd, 2017, p. 15.

93   M. Mukaida, Q. Wei and T. Ishida, *Synth. Met.*, 2017, **225**, 64–69.

94   K. Kirihara, Q. Wei, M. Mukaida and T. Ishida, *Synth. Met.*, 2018, **246**, 289–296.

95   Q. Wei, M. Mukaida, K. Kirihara, Y. Naitoh and T. Ishida, *RSC Adv.*, 2014, **4**, 28802–28806.

96   H. Fang, B. C. Popere, E. M. Thomas, C.-K. Mai, W. B. Chang, G. C. Bazan, M. L. Chabinyc and R. A. Segalman, *J. Appl. Polym. Sci.*, 2017, **134**, 44208.

97   A. K. Menon, O. Meek, A. J. Eng and S. K. Yee, *J. Appl. Polym. Sci.*, 2017, **134**, 44060.

98   A. K. Menon and S. K. Yee, *J. Appl. Phys.*, 2016, **119**, 55501.

99   N. Satoh, M. Otsuka, T. Ohki, A. Ohi, Y. Sakurai, Y. Yamashita and T. Mori, *Sci. Technol. Adv. Mater.*, 2018, **19**, 517–525.

100   R. R. Søndergaard, M. Hösel, N. Espinosa, M. Jørgensen and F. C. Krebs, *Energy Sci. Eng.*, 2013, **1**, 81–88.

101   K. Suemori, S. Hoshino and T. Kamata, *Appl. Phys. Lett.*, 2013, **103**, 153902.

102   M. Ishimaru, A. Kubo, T. Kawai and Y. Nonoguchi, *MRS Adv.*, 2019, **4**, 147–153.

103   K. Gordiz, A. K. Menon and S. K. Yee, *J. Appl. Phys.*, 2017, **122**, 124507.

104   S. Hwang, W. J. Potscavage, R. Nakamichi and C. Adachi, *Org. Electron.*, 2016, **31**, 31–40.

105   P. Sheng, Y. Sun, F. Jiao, C. Di, W. Xu and D. Zhu, *Synth. Met.*, 2014, **193**, 1–7.

106   Q. Wei, C. Uehara, M. Mukaida, K. Kirihara and T. Ishida, *AIP Adv.*, 2016, **6**, 045315.

107   Q. Wei, H. Suga, I. Ikeda, M. Mukaida, K. Kirihara, Y. Naitoh and T. Ishida, *Org. Electron.*, 2016, **38**, 264–270.

108   K. Kirihara, Q. Wei, M. Mukaida and T. Ishida, *Synth. Met.*, 2017, **225**, 41–48.

109   M. Mukaida, K. Kirihara and Q. Wei, *ACS Appl. ENERGY Mater.*, 2019, **2**, 6973–6978.

110   N. Sato and M. Takeda, in *ICT 2005. 24th International Conference on Thermoelectrics, 2005.*, 2005, p. 175.

111   Y. Iwasaki and M. Takeda, in *2006 25th International Conference on Thermoelectrics*, 2006, p. 562.

112   R. Tian, C. Wan, N. Hayashi, T. Aoai and K. Koumoto, *MRS Bull.*, 2018, **43**, 193–198.

113   T. C. Watson, J. N. Vincent and H. Lee, *Appl. Energy*, 2019, **239**, 898–907.

114   S. A. Afghan and H. Géza, *Energies*, 2019, **12**, 3873.
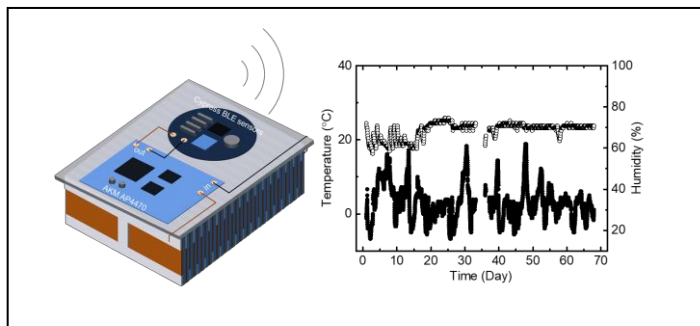
This perspective highlights recent pioneering studies revolving on the practical applications of organic thermoelectric devices.